University of Reading

Interface chemistry effects in nanofluids: Experimental and computational study of oil-based nanofluids with gold nanoplates

Article

Published Version

Creative Commons: Attribution-Noncommercial 4.0

Open Access

Carrillo-Berdugo, I., Sampalo-Guzmán, J., Grau-Crespo, R. ORCID: https://orcid.org/0000-0001-8845-1719, Zorrilla, D. and Navas, J. (2022) Interface chemistry effects in nanofluids: Experimental and computational study of oil-based nanofluids with gold nanoplates. Journal of Molecular Liquids, 362. 119762. ISSN 0167-7322 doi: https://doi.org/10.1016/j.molliq.2022.119762 Available at https://centaur.reading.ac.uk/106703/

It is advisable to refer to the publisher's version if you intend to cite from the work. See Guidance on citing.
Published version at: http://dx.doi.org/10.1016/j.molliq.2022.119762
To link to this article DOI: http://dx.doi.org/10.1016/j.molliq.2022.119762

Publisher: Elsevier

All outputs in CentAUR are protected by Intellectual Property Rights law, including copyright law. Copyright and IPR is retained by the creators or other copyright holders. Terms and conditions for use of this material are defined in the End User Agreement.

www.reading.ac.uk/centaur

University of Reading

CentAUR

Central Archive at the University of Reading

Reading's research outputs online

Journal of Molecular Liquids 362 (2022) 119762

Contents lists available at ScienceDirect

Journal of Molecular Liquids

journal homepage: www.elsevier.com/locate/molliq

Interface chemistry effects in nanofluids: Experimental and computational study of oil-based nanofluids with gold nanoplates

Iván Carrillo-Berdugo [a,b,*], Javier Sampalo-Guzmán [a], Ricardo Grau-Crespo [b], David Zorrilla [a], Javier Navas [a,*]

[a] Departamento de Química Física, Facultad de Ciencias, Universidad de Cádiz, E-11510 Puerto Real (Cádiz), Spain
[b] Department of Chemistry, University of Reading, Whiteknights, Reading RG6 6DX, United Kingdom

ARTICLE INFO

Article history:
Received 25 May 2022
Revised 27 June 2022
Accepted 29 June 2022
Available online 2 July 2022

Keywords:
Nanofluids
Specific heat
Thermal conductivity
Surface interactions
Au nanoplates

ABSTRACT

The chemistry of interfaces and its relation with energy storage at and transport through solid–liquid interfaces in heat transfer nanofluids is a very unexplored terrain. Here we discuss how the magnitude of the changes in specific heat and thermal conductivity of the base fluid, upon dispersion of a nanomaterial, depends on the surface chemistry of that nanomaterial. We focus on nanofluids with Au nanoplates from an integrated experimental and theoretical perspective, and compared our findings with those previously reported for nanofluids with Pd nanoplates in the same base fluid. Pd and Au are known to have different surface chemistry, and so are the structures of the solid–liquid interfaces and the thermal properties of these nanofluids. It was experimentally found that for mass fractions in the order of 0.01 wt%, Pd and Au nanoplates provide enhancements of 5.9% and 1.6% in specific heat, and enhancements of 12.5% and 17.9% in thermal conductivity, at 373 K. It was verified using density functional theory and classical molecular dynamics simulations that base fluid molecules can chemisorb on Pd surfaces, but not on Au surfaces. This work suggests that the stronger interactions between species at solid–liquid interfaces, the higher the specific heat enhancements and the lower the thermal conductivity enhancements at high temperature.

© 2022 The Author(s). Published by Elsevier B.V.

1. Introduction

Nanofluids (colloidal suspensions of nanomaterials) [1] have been widely studied for more than two decades by researchers motivated by their enhanced thermophysical properties over conventional heat transfer fluids [2], and potential applications, particularly, in solar energy conversion processes [3–13]. Concentrating solar power (CSP) is a renewable technology that can largely benefit from nanofluids, as heat transfer fluids (HTF), to improve the efficiency of solar-to-thermal-to-electric energy conversion. The eutectic and azeotropic mixture of 76.5% diphenyl oxide (DPO) and 26.5% biphenyl (BP), commercially available as Dowtherm^{TM} A, is the HTF of choice for this application for its thermal stability, low vapour pressure, low viscosity and non-corrosive behaviour, but it also has low specific heat and thermal conductivity [14].

A plethora of nanostructured materials have been proposed to be used as disperse phase in nanofluids, but those of metallic character have received more attention in literature for their high thermal conductivity. The adsorption of organic molecules on transition metals, especially those with aromatic substituents like DPO and BP, are of great interest for the formation of self-assembled monolayers that define a very unique interface. The interface between transition metals and high π-electron density species has captivated research attention for their application in electronics, biosensing, catalysis or, as in the present case, energy storage [15]. The concept of an interfacial layer of base fluid around the dispersed nanomaterials has become a quintessential element for the explanation of the anomalous enhancements (usually higher than expected for the concentration of nanomaterial) in properties like specific heat and thermal conductivity [16–22]. However, no definitive answers have been provided on the nature of interactions at the solid–liquid interface, the thermodynamic and kinetic requirements for the existence of that layer or the relation of causality between this layer and the observables of interest. Understanding these issues and the implications for the measurable physical properties is central to achieve a rational control of the properties of nanofluids and progress towards their maximum potential in applications [23].

Computer simulations are very useful to rationalise the behaviour at the nanoparticle/molecular interface from a microscopic picture. Granatier et al. [15] have studied the interactions between

* Corresponding authors at: Departamento de Química Física, Facultad de Ciencias, Universidad de Cádiz, E-11510 Puerto Real (Cádiz), Spain.
E-mail addresses: ivan.carrillo@uca.es (I. Carrillo-Berdugo), javier.navas@uca.es (J. Navas).

https://doi.org/10.1016/j.molliq.2022.119762
0167-7322/© 2022 The Author(s). Published by Elsevier B.V.

Pd, Ag and Au atoms and benzene, coronene and graphene, using plane-wave density functional theory (DFT) calculations. They found that the nature of chemical bonding to these high π-electron density species is very different depending on the metal. For instance, the bonding of Pd is predominantly covalent, whereas the bonding of Au is the result of charge transfer, dispersion interactions and relativistic effects. If Pd or Au nanostructures were dispersed in the aforementioned mixture of DPO and BP, these molecules should be expected to chemisorb on Pd surfaces and to physisorb on Au surfaces. In such case, different interfaces would be generated and different physical properties should be expected for the corresponding nanofluid. Our research proposal relies on this premise. In previously published research [24–26], we prepared and characterised Pd nanoplate-containing nanofluids and reported increments in specific heat and thermal conductivity with mass fractions in the order of 10^{-2} wt%. It was proven by DFT and molecular dynamics (MD) calculations that chemisorption of BP molecules on Pd surfaces is thermodynamically and kinetically favoured, and that the formation of a layer of chemisorbed molecules is directly responsible of the large increase in specific heat and modest increase in thermal conductivity. Here, we report on experimental and DFT/MD results for Au nanoplate-containing nanofluids, with the same base fluid and mass fractions in the same order of magnitude. The differences in the chemistry and structure of interfaces and physical properties of interest between these two metals are pointed out. Recurring comparisons between both colloidal systems allow to draw a big picture of the role of the chemistry of interfaces on defining the properties of heat transfer nanofluids.

2. Methodology

2.1. Experimental framework

Nanofluid samples were prepared following a two-step procedure: (i) synthesis and isolation of the nanomaterial and (ii) dispersion of the as-synthesised nanomaterial into the base fluid.

In the first step, Au nanoplates were synthesised via kinetically controlled reduction of $[AuCl_4]^-$. Typically, 11.0 ml of a freshly prepared aqueous solution 17.4 mM in $HAuCl_4$ (Sigma-Aldrich©, 99.9%), 1.2 mM in PVP_{40k} (Sigma-Aldrich©, ave. mol. wt. 40 kDa) and 1.0 mM in KCl (Sigma-Aldrich©) are stirred at 300 rpm for 24 h in a round-bottom flask at 30 °C under air atmosphere. In this synthetic scheme, PVP plays a role as mild reducing agent [27]. Kinetics of reduction are further controlled by Cl^- anions, whose preferential adsorption on (1 1 1) surfaces inhibits growth along the [1 1 1] direction, thus leading to the formation of the plate-like morphology [28]. The solid product was collected by centrifugation, rinsed twice with ethanol and once with acetone to remove all inorganic and organic residual species, and dried in vacuum at 60 °C for 48 h. Morphology, crystalline structure and oxidation state of the synthesised nanostructured material were verified by transmission electron microscopy (TEM) (FEI©, Talos F200S), X-ray diffraction (XRD) (Bruker©, D8 Advance A25, Cu-Kα source, LYNXEYE detector) and X-ray photoelectron spectroscopy (XPS) (Physical Electronics©, PHI 5000 VersaProbe II, Al-Kα source).

In the second step, 51.6 mg of Au nanoplates (in powder form) were added to 100 ml of a 1 wt% solution of Triton™ X-100 (Panreac©) in Dowtherm™ A (The Dow Chemical Company©) and dispersed by pulsed ultrasonication (Sonics&Materials©, VCX-500, 13 mm tip, 2/4 s on/off pulse time, 50% amplitude) for 3 h. By doing so, a fine stock suspension was prepared and divided into two more fractions for dilution. These are the nanofluid samples to be characterised, with mass fractions of $4.8{\cdot}10^{-2}$ wt%, $2.4{\cdot}10^{-2}$ wt% (1:2 dilution) and $9.7{\cdot}10^{-3}$ wt% (1:5 dilution) in Au nanoplates, together with the base fluid (Dowtherm™ A) and the host fluid (the 1 wt% solution of Triton™ X-100 in Dowtherm™ A). Specific heat was determined by temperature-modulated differential scanning calorimetry (TMDSC) (Netzsch©, DSC 214 Polyma, closed concavus pan), from a temperature ramp from 288 K to 378 K (the maximum temperature of operation for the fluid to be in liquid phase at 1013 hPa) at 1 $K{\cdot}min^{-1}$, with a modulation of ± 1 K in amplitude and 120 s in periodicity. TMDSC measurements were performed in triplicate. Thermal conductivity was measured using the transient hot-bridge technique with a hot point sensor (THB-HPS) (Linseis©, THB-100, sensor type C), with a measurement time of 10 s for an input power of 32 mW, with a delay of 30 s between replicas. Samples were contained in cylindrical glass vials, with 2.5 ml of capacity, and hold in individually jacketed vessels in a dry block heater (IKA®, DB 5.2) at 298 K, 323 K, 348 K and 373 K. Up to ten replicas were recorded for each sample and temperature in THB-HPS measurements.

2.2. Theoretical framework

Geometry optimisations and energy calculations for different adsorption complexes were run, at the DFT level-of-theory, using the Vienna *Ab initio* Simulation Package (VASP) [29–32]. Surface models are represented by supercells in which Au (1 1 1) and Au (1 0 0) surface terminations are limited by a vacuum slab of 15 Å that minimises unphysical interactions between periodic images in the surface normal direction. Adsorption sites on Au surfaces are described in Section I of the Supplementary Material (SM). Here the Perdew-Burke-Ernzernhof (PBE) functional [33,34], in which the exchange–correlation energy term is described by the generalised gradient approximation (GGA), was used to solve Kohn-Sham equations. The Grimme's dispersion correction method (D3) [35] was also included for an adequate description of van der Waals interactions, which play a key role on adsorption. The GGA-PBE-D3 functional has been proven to work well for the calculation of adsorption energies of molecules on metal surfaces [36] Valence wavefunctions were described by sets of planewaves with kinetic energies up to 400 eV (extended up to 520 eV for the Au unit cell optimisation). Interactions between valence electrons and ionic cores were described using the projector-augmented wave (PAW) pseudopotentials [37,38]. Brillouin-zone integrations were performed using Γ-centred k-point grids generated by the Monkhorst-Pack method [39,40], with a k-point density of 0.2 $Å^{-1}$ along periodic directions in the reciprocal space (a single k-point was considered for the imposed non-periodic direction). The Methfessel-Paxton smearing method [41], with an electronic temperature σ of 0.2 eV, was used to describe orbital occupancies during calculations. We verified energy calculations with these parameters led to well-converged energy values, with a difference between $U(\sigma)$ and $U(\sigma \rightarrow 0)$ below 1 meV per atom.

The activation energy for adsorption was also calculated from the minimum energy path (MEP) for the adsorption of BP and DPO on Au (1 1 1) and (1 0 0), which are computed using the nudged elastic band (NEB) method [42,43] available in VASP. NEB images were kept equidistant during energy minimisation until the total free energy difference between ionic steps was smaller than 0.01 eV. All considerations for geometry optimisation and energy calculation of adsorption complexes were also applied for NEB simulations.

MD simulations were used to investigate the contribution of Au nanoplates to the thermophysical properties of these nanofluids. Molecular models details, the explicit form of the functional of classical potentials [44–49] that was used to describe the energetics of bonding and non-bonding interactions between atoms in MD, and a discussion about its adequacy and limitations to accurately reproduce the physical properties of interest as a function

of temperature, are all given in Section II of the Supplementary Material. The Large Atomic/Molecular Massively Parallel Simulator (LAMMPS) [50,51] is the classical MD code of choice for running the required simulations. The initial configurations were created with Moltemplate [52,53], a text-based molecular builder for LAMMPS. Periodic boundary conditions are imposed in all directions. Lennard-Jones pairwise interactions are limited to a cut-off distance of 10 Å. The particle–particle particle-mesh (PPPM) summation method [54] was applied to compute long-range electrostatics. The Verlet integration scheme [55] is used with a timestep of 1 fs. Velocities are rescaled with the Nosé-Hoover thermostat and barostat algorithms [56–59]. The simulation run, with the above set-up, includes (i) a 300 ps run in NVE for relaxation, (ii) a 500 ps run in NVT for temperature equilibration, (iii) a 1.0 ns run in NPT for pressure and temperature equilibration, (iv) a 1.0 ns run in NVT for the computation of specific heat and radial distribution functions and coordination numbers, and (v) a 5.0 ns run in NVT for the computation of thermal conductivity. The trajectories of the base fluid model and the nanofluid model are all computed with this scheme at 298 K, 323 K, 348 K and 373 K and 1013 hPa (in line with experimental conditions). Specific heat was calculated from the total energy variance using a fundamental relation of Statistical Mechanics for canonical ensembles [60]. Thermal conductivity and dynamic viscosity were computed using the Green-Kubo integrals [61,62] over a dataset of 1000 correlation points distributed with a sampling interval of 5 fs (correlation time equals 5 ns).

3. Results and discussion

3.1. Characterisation of Au nanoplates

Fig. 1A shows representative TEM images of the as-synthesised nanopowder. About 30% of the nanostructures are identified to have the desired plate-like morphology, with hexagonal or truncated triangular contours. Electron transparency is verifiable in most cases, which suggests these are quasi-2D nanostructures. Edge length varies within 200 nm and 800 nm. The diffractogram in Fig. 1B fulfils the Bragg condition for 2θ equal to 38.2°, 44.4°, 64.6°, 77.6° and 81.7°, which matches the expected angles for maximum diffracted intensity from (111), (200), (220), (311) and (222) planes in a face-centred cubic Au crystalline structure. The relatively higher intensity from (111) planes is a consequence of nanoplates being faceted by (111) planes on top and bottom surfaces (as it has been previously described for nanoplates of face-centred cubic metals) [63–65], which inevitably imposes a preferential orientation for diffraction. Lastly, the oxidation state of Au is verified on the basis of an XPS analysis. The general survey spectrum is available in Fig. 1C, together with an inset for the high-resolution survey of the Au 4f region, which is the primary signal for the assignment of Au metal. Here the Au $4f_{7/2}$ and Au $4f_{5/2}$ spin–orbit components are identified, at 84.1 eV and 87.8 eV, respectively. The binding energy for Au $4f_{7/2}$, a chemical shift of 3.7 eV between spin–orbit split peaks and the asymmetric peak shapes confirmed the chemical state of Au in the nanoplates is, indeed, metallic [66].

Overall, this structural and compositional characterisation by TEM, XRD and XPS confirms that quasi-2D plate-like Au nanostructures have been successfully synthesised in a significant proportion. This achievement is central for the present paper, because the nanoplate morphology has a large specific surface area available for base fluid molecules to interact with upon dispersion. If interactions at solid–liquid interfaces are sufficiently strong for adsorption to occur and the properties of the adsorbed fluid are different to the bulk fluid, then a large solid–liquid interface should significantly contribute to the overall nanofluid properties.

3.2. Specific heat and thermal conductivity of Au nanoplate-containing nanofluids

Specific heat, c, and thermal conductivity, κ, are the physical properties ruling heat storage and transfer. For that, these are the most studied properties of nanofluids for energy conversion and thermal management application, and are frequently included as dominant factors in figures-of-merit assessing their performance for such purpose. Here, we characterised these two physical properties of the base fluid, the host fluid and all nanofluid samples.

Fig. 2A shows specific heat values, as a function of temperature. The measured specific heat values for the base fluid are verified to be in good agreement compared to the reference specific heat values provided by the supplier, with a maximum relative deviation below 1.7%. The addition of Triton^{TM} X-100 (1.0 wt%) is determined not to cause a measurable change in specific heat, as the difference between the specific heat values of the host fluid and the base fluid are not discernible from the standard deviation of the measurements. Alternatively, the addition of Au nanoplates is found to significantly increase the specific heat of the base fluid by a maximum

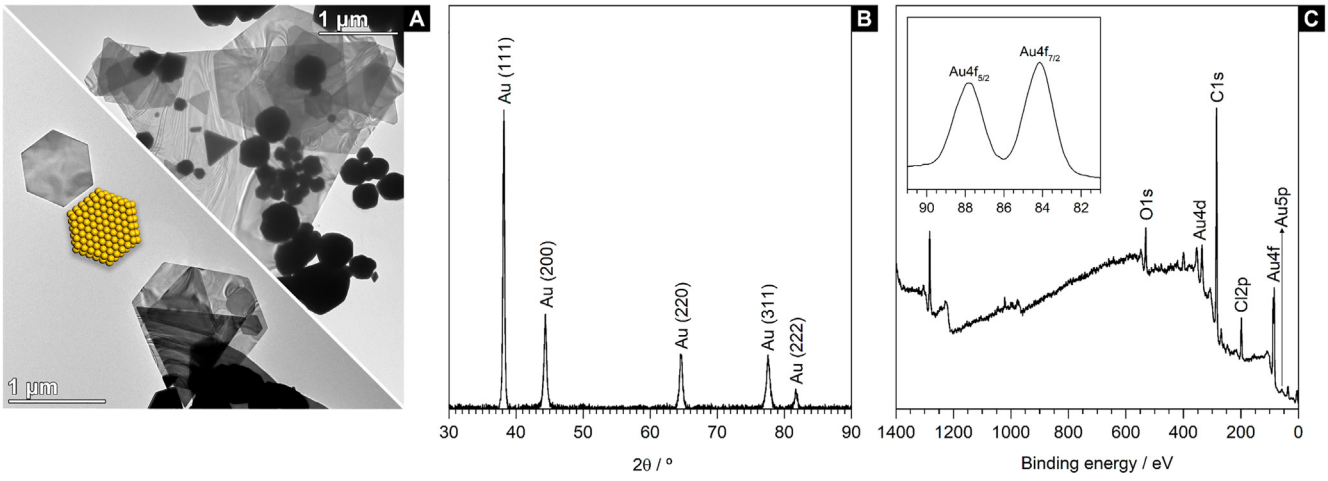

Fig. 1. Structural and compositional characterisation of Au nanoplates: typical TEM images [A], X-ray diffractogram [B], and X-ray photoelectron spectrum [C] for the as-synthesised Au nanopowder. All signals in [C] are conveniently referenced to the C 1 s transition, at 284.8 eV, assigned to adventitious carbon. The inset in [C] shows a high-resolution scan of the Au 4f region.

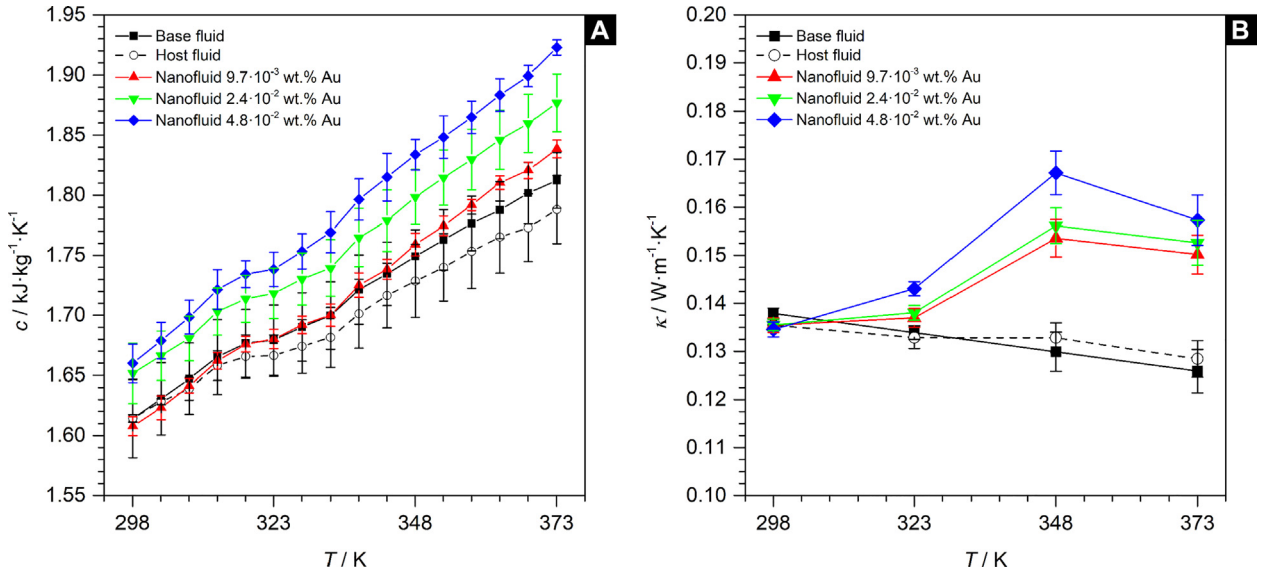

Fig. 2. Specific heat [A] and thermal conductivity [B] as a function of temperature. Solid lines do not represent actual data but are included as guide to the eye.

6.1 ± 1.4%, at 373 K, for a mass fraction of $4.8{\cdot}10^{-2}$ wt%. The fact that the specific heat of the nanofluid is higher compared to that of the base fluid is a remarkable observation, and a contradiction to predictions made by the weighted average rule. According to this rule, a decrease in specific heat should be expected for increasing mass fractions of solid, as the specific heat of solids is typically lower than that of this base fluid. The problem here is that this rule, although widely used in this context, is valid for ideal gases only, and nanofluids are far from mixtures of non-interacting chemical species. The interactions between species at solid–liquid interfaces are, in fact, the root cause for specific heat enhancement in some nanofluids, as it was previously proven for Pd nanoplate-containing nanofluids [24,25]. We will go back to this issue, with more details, in the theoretical part of this paper.

Fig. 2B shows thermal conductivity values, also as a function of temperature. In the absence of a liquid-phase primary reference standard, the base fluid was used as a reference to correct deviations in the measurement of the apparent thermal conductivity due to natural convection. As for specific heat, the addition of Triton™ X-100 (1.0 wt%) is determined not to change the thermal conductivity of the base fluid. The addition of Au nanoplates enhances it by a maximum 24.9 ± 6.1%, at 373 K, for a mass fraction of $4.8{\cdot}10^{-2}$ wt%. Increasing mass fraction of the nanomaterial affects the behaviour for increasing temperatures, even though the base fluid is still the majority component. This behaviour was also observed with Pd nanoplates in the same fluid [26]. Enhancements in thermal conductivity are likely expected because the thermal conductivity of Au nanoplates (and that of any other elemental metal) is much higher than that of this base fluid. However, such enhancements surpass the predictions of the effective medium theory of Maxwell [67], an observation that has been previously raised by many other authors, as pointed out by Mugica and Poncet [20]. These two authors also emphasised the importance of particle aggregation for the anomalous thermal conductivity of nanofluids, and postulated the complex dynamics of aggregations and interactions between species at solid–liquid interfaces as sources of disparity in the measurement of thermal conductivity. We will go back to the latter issue in the theoretical part of this paper.

3.3. Modelling the Au-molecular interface with DFT simulations

The above reported experimental results reveal a significant increment in thermal conductivity accompanied by a small gain in specific heat in Au nanoplate-containing nanofluids with respect to their base fluid. Interactions in solid–liquid interfaces are known to be responsible of specific heat increases in nanofluids if chemisorption of base fluid molecules at the solid–liquid interface occurs, as it was previously reported for nanofluids with Pd nanoplates in the fluid mixture of BP and DPO [24–26]. It seems not be the case for Au nanoplate-containing nanofluids. Compared to other *d*-metals like Pd, the chemistry of Au is much depleted by its [Xe] $4f^{14}\ 5d^{10}\ 6\ s^1$ electronic configuration, with a half-full *s* and full *d* valence subshells, and the relativistic contraction of the 6 *s* orbital and the chemical inertia of any electron occupying it, but the consequent expansion of 5*d* orbitals is of particular importance for certain reactivity [68]. Dismissing the possibility of chemisorption of BP and DPO molecules on Au surfaces, although likely for the findings on specific heat, may be a misguided *a priori* assumption. We therefore investigated the structure and adsorption energy of several adsorption complexes of BP and DPO on Au (111) and Au (100) surfaces via DFT simulations with VASP.

Several initial geometries have been considered in this study, each one representing a different adsorption complex. In most of them both phenyl rings in BP and DPO molecules lie parallel to high symmetry sites at the metal surface, as it favours the alignment of the C p_z orbitals to overlap with Au d_z^2 and d_{yz} orbitals for π-bonding, as it occurs with benzene on Au surfaces. These sites are usually notated as Bri (four-bridging atoms), H_{hcp} (for hexagonal close-packed hollow), H_{fcc} (face-centred cubic hollow) or T (on the top of an atom) at (111) surfaces, and H_{bcc} (body-centred cubic hollow), $Bri_{1/2}$ (two-bridging atoms) or T at (100) surfaces (see Section I of the Supplementary Material). Rings at (111) surfaces may occupy those sites with two possible orientations, rotated 0° or 30° with respect to lattice vectors. Another initial geometry considers the possibility of DPO approaching surfaces by the O atom. A total of 44 non-redundant initial configurations have been submitted for geometry optimisation by energy minimisation. Fig. 3

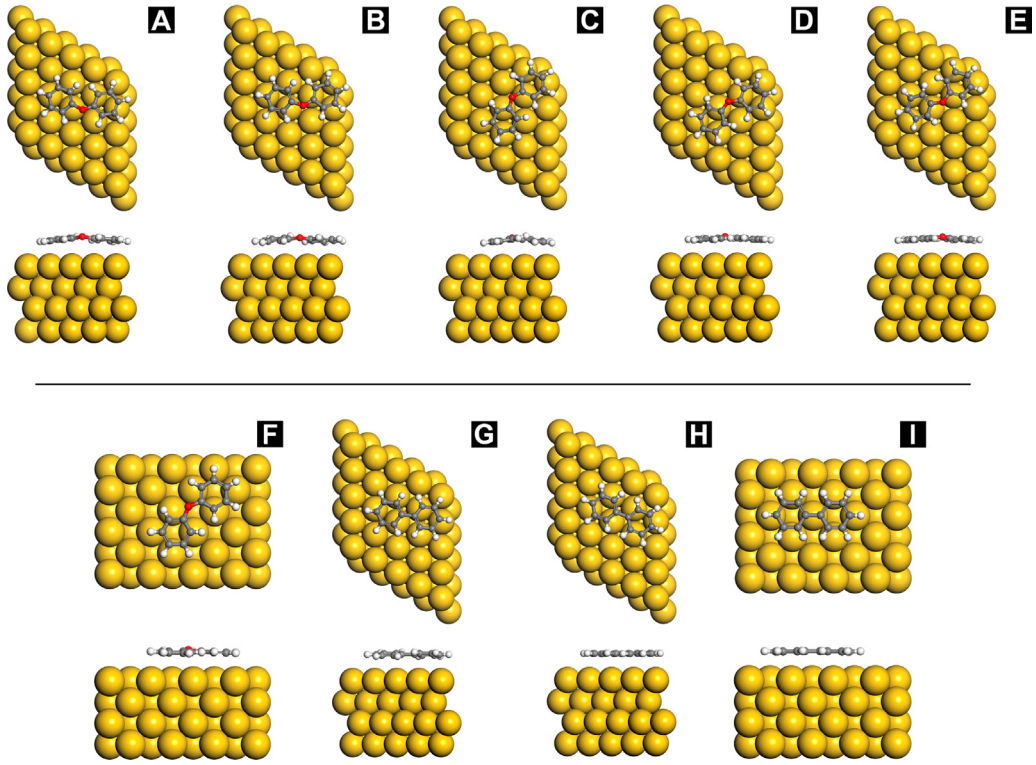

Fig. 3. Geometry of most stable adsorption complexes for DPO on Au (1 1 1) [A-E], DPO on Au (1 0 0) [F], BP on Au (1 1 1) [G, H] and BP on Au (1 0 0) [I]. Supercells are visualised along the perpendicular and parallel directions to the surface termination (top and bottom images, respectively). Notation for each geometry is provided in Table 1.

shows the most stable adsorption complexes derived from DFT calculations. The initial configurations converged to one out of the nine structures in Fig. 3, or exhibited a much weaker adsorption than these (like the one approaching by the O atom).

The geometry and energy of the most stable adsorption complexes in Fig. 3 has been examined and summarised in Table 1, in which complexes for a given molecule are listed by increasing energy. The negative sign of adsorption energies indicates that the adsorption of BP and DPO on either Au (1 1 1) or Au (1 0 0) surfaces is thermodynamically favoured, regardless of which sites are occupied. The magnitude of adsorption energies demonstrates the stability of these adsorption complexes, whose release from the surface is expected to be energetically prohibitive, given the energetics of thermal effects are in the order of k_BT, which is 58 meV at 673 K, the maximum operating temperature for the base fluid. The relative stability of the different adsorption complexes is geometry dependent. In terms of surface geometry, the more Au atoms are simultaneously coordinated by a phenyl ring on a given site (up to four in Bri_4 and H_{bcc} sites and up to three in H_{hcp} and H_{fcc} sites), the stronger adsorption. In terms of molecule geometry, significant distortions are found for the C–O–C angle in DPO (130.0° in adsorption complexes, 117.2° in gas phase) and the C═C—C═C dihedron in BP (180.0° in adsorption complexes, 144.5° in gas phase), although bond lengths in both DPO and BP and the C—O═C═C dihedron in DPO are preserved. No significant differences were found for molecules adsorbed on different surfaces. This is a remarkable different situation compared to Pd surfaces, in which molecular geometry, even the C═C bond length, was remarkably distorted due to chemisorption [24]. Overall, the more gas-phase geometry is preserved, the lower energy penalty, unless a planar conformation is achieved by adsorption, which results into electron delocalisation [69] and further stabilisation. That is the case

Table 1
Adsorption energy and geometry descriptors for structures in Fig. 3.

Structure		*site A*	*site B*	E_{ads}[a] / *eV*	N_{Au}[b]	d_{AuC}[c] / *Å*
DPO on Au (1 0 0)	[F]	H_{bcc}	H_{bcc}	−1.55	8	2.88
DPO on Au (1 1 1)	[B]	Bri^{30°	$H^{0^\circ}_{hcp}$	−1.49	7	3.06
	[C]	Bri^{30°	$H^{0^\circ}_{fcc}$	−1.48	7	3.08
	[A]	Bri^{30°	Bri^{30°	−1.47	8	3.08
	[D]	$H^{0^\circ}_{hcp}$	$H^{0^\circ}_{hcp}$	−1.46	6	3.06
	[E]	$H^{0^\circ}_{fcc}$	$H^{0^\circ}_{fcc}$	−1.45	6	3.07
BP on Au (1 0 0)	[I]	H_{bcc}	H_{bcc}	−1.67	8	2.86
BP on Au (1 1 1)	[H]	$H^{0^\circ}_{hcp}$	$H^{0^\circ}_{fcc}$	−1.60	6	3.03
	[G]	Bri^{30°	Bri^{30°	−1.59	8	3.04

[a] Adsorption energy, calculated as the energy difference between the adsorption complex and the sum of the energies of the isolated surface and the gas-phase molecule.
[b] number of Au atoms implicated in the surface-molecule interaction.
[c] interplanar distance between the surface and the mean plane defined by phenyl rings in molecules.

of BP on $H_{bcc} - H_{bcc}$ sites at Au (100) and $H^{0^\circ}_{hcp} - H^{0^\circ}_{fcc}$ sites at Au (111) (images [I] and [H] in Fig. 3).

The nature of interactions driving the adsorption process is of particular importance for further modelling using MD. Comparing our findings on the adsorption of BP and DPO on Au (111) and Au (100) surfaces with those for the adsorption of these molecules on Pd (111) and Pd (100) surfaces [24] could be useful for such purpose. The adsorption of BP and DPO on these surfaces is significantly different, but so is the chemistry of these surfaces. The electronic configurations of Pd ([Kr] $4d^{10}$ 5 s^0) and Au ([Xe] $4f^{14}$ $5d^{10}$ 6 s^1) make clear that the acceptance of π electrons from phenyl rings is very much likely in Pd than Au. Besides, the particularly large metallic radius of Au atoms (1.45 Å in Au fcc unit cell, optimised with VASP) compared to that of Pd atoms (1.37 Å in Pd fcc unit cell, optimised with VASP under the exact same conditions) makes the symmetry match and orbital overlap worse for phenyl rings on Au surfaces than Pd surfaces (this is evidenced by the displacement of geometry centres between phenyl rings and adsorption sites in Fig. 3). As a result, DFT simulations predicts that the magnitude of adsorption energies on Au surfaces (between −1.7 eV and −1.4 eV) are much smaller than those on Pd surfaces (between −4.7 eV and −3.5 eV), whereas the distances between phenyl rings and the metallic surface is much wider at Au surfaces (~2.9 Å) than Pd surfaces (~2.2 Å). All the above represents sufficient evidence for us to safely conclude that the adsorption of BP and DPO on Au surfaces, in which no chemical interactions beyond strong van der Waals interactions should be expected, is weaker than on Pd surfaces, in which chemical bonding is predicted. The BP and DPO should therefore be expected to form a layer of physisorbed molecules covering the Au nanoplate surfaces, in contrast to the layer of chemisorbed molecules that was predicted to be formed on Pd nanoplate surfaces. Different surface chemistry results into different interfacial layers.

We have also estimated the kinetic barriers for physisorption, using NEB calculations to approximate the MEP for the adsorption of BP and DPO on Au surfaces at the most stable configurations (that is, $H^{0^\circ}_{hcp} - H^{0^\circ}_{fcc}$ for BP on Au (111), $H_{bcc} - H_{bcc}$ for BP on Au (100), $Bri^{30^\circ}_{4} - H^{0^\circ}_{hcp}$ for DPO on Au (111) and $H_{bcc} - H_{bcc}$ for DPO on Au (100)). Fig. 4 shows the computed MEP for all these cases. Activation energies are estimated to be 5.9 meV for BP on Au (111), 9.6 meV for BP on Au (100), 13.3 meV for DPO on Au (111) and 22.1 meV for DPO on Au (100). We invoke again the fact that the energetics of thermal effects are in the order of the k_BT product, which is equal to 25 meV at 298 K, meaning both molecules can physisorb freely on both surfaces, with no kinetic hindrance at room temperature. This is another remarkable difference with respect to Pd surfaces, in which the adsorption of DPO was kinetically hindered (with activation energies in the order of 0.2–0.3 eV) and only BP was expected to chemisorb without activation barrier.

3.4. Molecular dynamics of Au nanoplate-containing nanofluids

We now know from our DFT simulations that no chemistry beyond van der Waals interactions should be expected to occur between the Au nanoplate and the fluid molecules. Therefore, the Lorentz-Berthelot combining rules can also be used as a first approximation to parametrise the Lennard-Jones potential describing intermolecular interactions between species at the solid–liquid interface. We will open this section by describing the molecular architectures at equilibrium using radial distribution functions and coordination numbers to elucidate if the resulting Lennard-Jones potential reproduces the expected physisorption-ruled interface. We are particularly interested in the molecular radial distribution functions, $G(r)$, and the molecular coordination numbers, $N(r)$, as descriptors for molecular structures in space.

Fig. 5A shows both the $G(r)$ for DPO and BP, as a function of the distance to Au atoms, at different temperatures. There is a series of peaks with locally higher probabilities at distances beyond 2.0 Å that are indicative of structural order around the nanoplate, and suggest that the physisorption-ruled interface scenario predicted by DFT simulations is well described in MD simulations too. All probabilities within the interfacial region and its vicinity are below 1.0, as expected for a system in which no ties due to chemical bonding between species at this region exist.

Fig. 5B shows the $N_{DPO}(r)/N_{BP}(r)$ ratio, at different temperatures too. This ratio is approximately 2.77 in the bulk fluid, which is nearly preserved for distances beyond 5.0 Å from the Au nanoplate surface. According to our findings (in Fig. 4) from DFT simulations, the activation energies for adsorption are sufficiently small for the adsorption of both molecular species to occur and for the sticking probabilities to be very much determined by the relative proportion of these species in the fluid. Therefore, this $N_{DPO}(r)/N_{BP}(r)$ ratio should be expected to be equal to 2.77 in the interfacial region too, but it locally increases, which reveals a preferential approach of

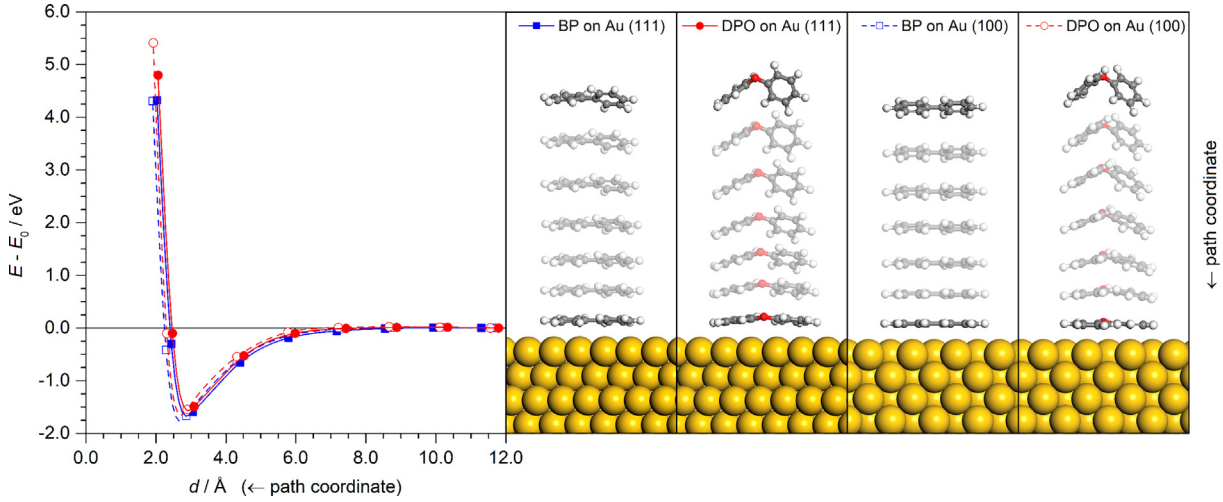

Fig. 4. Computed MEP for the adsorption of BP and DPO molecules on Au (111) and (100) surfaces. Free and adsorbed structures are highlighted. All energies are given relative to their corresponding first image in the NEB calculation.

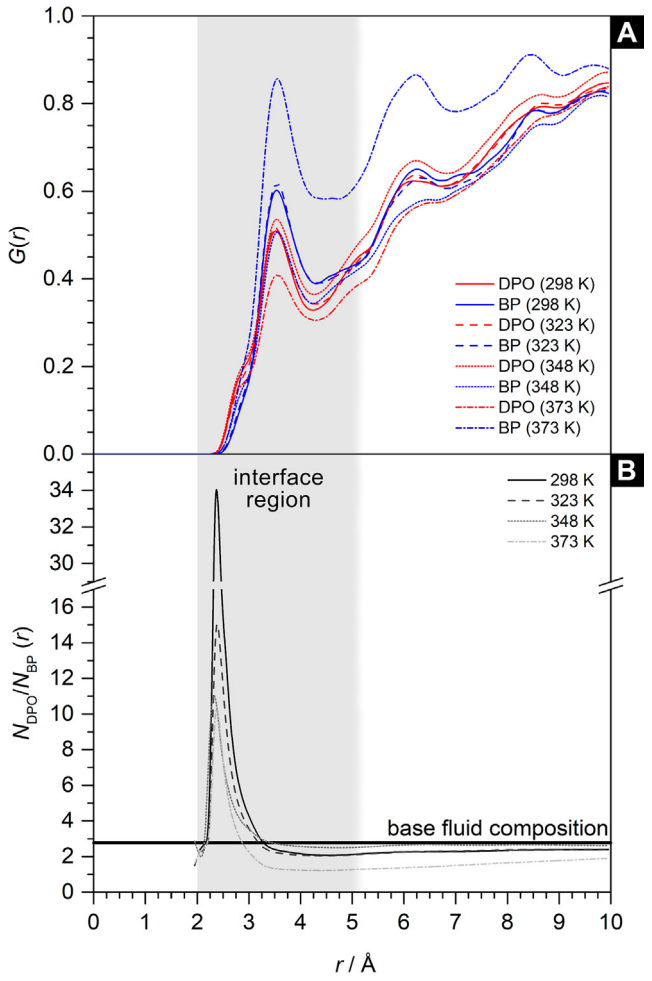

Fig. 5. Molecular radial distribution functions [A] and the DPO-to-BP ratio of coordination numbers [B], as a function of the distance from Au atoms.

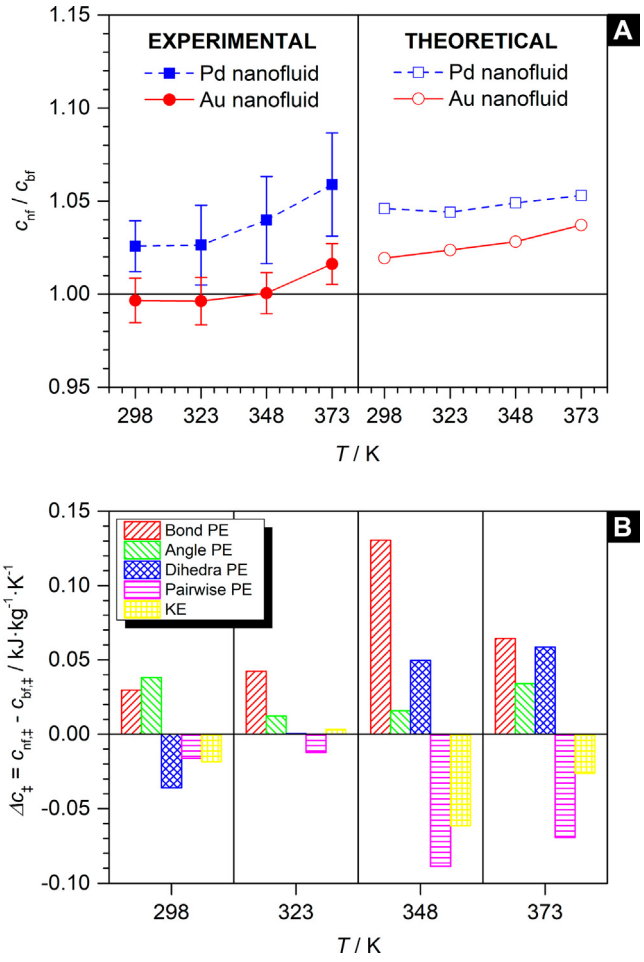

Fig. 6. Experimental and theoretical specific heat enhancements of Pd and Au nanofluids with respect to the base fluid [A], and contributions to the total specific heat from different energy partitions in Au nanofluid MD models [B], as a function of temperature. Experimental values in [A] are referred to nanofluids with mass fractions of $1.2{\cdot}10^{-2}$ wt% in Pd nanoplates and $1.0{\cdot}10^{-2}$ wt% in Au nanoplates. Solid lines do not represent actual data but are included as guide to the eye.

DPO to the Au nanoplate in MD simulations. The ease of approach for DPO is likely a consequence of its less restrictive rotational profile, as both aromatics rings are indirectly linked by an ether-like O-atom.

The specific heat, c, can now be calculated from energy fluctuations in the system at constant volume and temperature, using the equation:

$$c = \frac{\langle E_T^2 \rangle - \langle E_T \rangle^2}{k_B T^2} = \frac{\sigma^2(E_T)}{k_B T^2} \quad (1)$$

which is a fundamental relation from statistical mechanics for the canonical ensemble (NVT) [60], where $\sigma^2(E_T)$ is the total energy variance. Systems at constant volume are incompressible, therefore no distinction for isobaric or isochoric specific heats has to be made here. The ratio of the computed values of c for the nanofluid and the base fluid models are plotted in Fig. 6A, which evidences an enhancement for the specific heat of the fluid, over the entire range of temperatures, in presence of the Au nanoplate and no chemically bonded species on its surface, but that enhancement is smaller than the one predicted in our previous works [24,25] in presence of a Pd nanoplate and chemisorbed BP molecules on its surface. Although the absolute c values are systematically overestimated in MD simulations (for the reasons stated in Section II of the Supplementary Material), the increments predicted are consistent and in good agreement with those find in our experiments for both nanofluids.

In previous work from our group [25] we analysed the contributions to the specific heat of the system, $\Delta c_{\ddagger}$, from different energy partitions denoted by ‡, as shown in Fig. 6B, and created a framework for their interpretation. $G(r)$ and $N_{DPO}/N_{BP}(r)$ in Fig. 5 already revealed that the presence of the Au nanoplate imposes a long-range order in the surrounding fluid, because Lennard-Jones interactions between species at the solid–liquid interface are stronger than Lennard-Jones and Coulomb interactions between species in the bulk fluid. This order restricts the translational motion and distorts the geometry of molecules at the adsorbed layer and secondary solvation layers, compared to those in the bulk fluid. For all that, the nanofluid model with the Au nanoplate exhibits less pairwise potential energy and kinetic energy variability, ($\Delta c_{PPE} < 0$ and $\Delta c_{KE} < 0$), but more bond, angle and dihedra potential energy variability ($\Delta c_{BPE} > 0$, $\Delta c_{APE} > 0$ and $\Delta c_{DPE} > 0$), with respect to the base fluid model. Thus, we have evidence to believe that additional energy storage in nanofluids with Au nanoplates is available in these layers, even if they are induced by van der Waals forces only. These layers were also recognised to be responsible for energy storage in a nanofluid model with a Pd nanoplate (in the same base fluid) [25], but chemical bonding between species at the solid–liquid interface ($\Delta c_{BPE} \gg 0$), the consequent distortion of nanoplate surfaces and chemisorbed molecules ($\Delta c_{BPE} \gg 0$ and $\Delta c_{DPE} > 0$), and the shielding these molecules impose for pairwise

interactions with the rest of the fluid ($\Delta c_{PPE} > 0$ and $\Delta c_{KE} > 0$) leads to higher energy storage. The comparisons between these two systems with different chemistry allows us to conclude that the stronger the interactions at solid–liquid interfaces, the greater the enhancement in specific heat.

The other property of interest is the thermal conductivity, κ. Solid-liquid interfaces play a key role not only for energy storage but also for energy transfer, as reported in previous literature. This transport property was computed using the Green-Kubo formalism [61,62], based on the integrals of time auto-correlation functions:

$$\kappa = \frac{V}{k_B T^2} \lim_{t\to\infty} \int_0^t \langle \vec{J}(0) \cdot \vec{J}(t) \rangle \mathrm{d}t \quad (2)$$

where $\langle \vec{J}(0) \cdot \vec{J}(t) \rangle$ is the heat flux vector auto-correlation (HFAC) functions. In Fig. 7A we show the ratio of the computed thermal conductivity values for the nanofluid and the base fluid models. MD simulations predict increasing thermal conductivity values for increasing temperatures in nanofluids, which is a consistent trend compared to the experimentally measured values for this property. The fact that thermal conductivity is slightly more sensitive to changes in temperature (higher positive slope) in presence of the Au nanoplate, with no chemically bonded species on its surface, compared to the Pd nanoplate, with chemisorbed BP molecules on its surface, is also a finding in good agreement with experiments. It is suggested that base fluid molecules that are chemically bonded at the interface distort the atomic-level structure of the nanoplate surface, thus interrupting the propagation of thermal vibrations, as it happens to be the case with Pd nanoplates. Interfacial layering is a shelter-like boundary of high thermal resistance that hinders heat conduction. The magnitude of the enhancement is, however, much higher than expected in both cases due to the enormous mass of the metal nanoplates with respect to the total mass of the simulation cell, whose total mass fractions are larger, by two orders of magnitude, than that of the characterised samples. The size of the simulation cell is necessarily restricted for MD simulations to be run with the available computational resources and time. The discussion is intended for qualitative purposes only.

We are now attending to the HFAC functions looking for additional insights on heat conduction. Fig. 7B compares HFAC functions from the base fluid model and the nanofluid model with the Au nanoplate at all temperatures. As originally described by McGaughey and Kaviany [70,71], the HFAC functions are fundamentally a linear combination of damped harmonic oscillators. While decaying to zero, the HFAC functions exhibit an overall behaviour resulting from the superposition of vibrations associated to many-body interactions in the system (represented by harmonic potentials or Morse potentials, which effectively are also harmonic potentials at the temperatures we study), and so to the back-and-forth oscillations responsible of energy transfer within the system. The amplitude decay is associated to heat transfer between molecules and so to the dissipation of heat in the fluid; that is the physical meaning of correlation loss in these functions. Dissipation becomes more evident in the integrals of HFAC functions, which are shown in Fig. 7C. Heat is rapidly dissipated in liquids due to the short mean free-path of thermal vibrations in the fluid, so that HFAC functions are quickly damped. As a consequence, the integrals from the base fluid model saturate at very short times, and low thermal conductivity values are found at all temperatures. The decreasing thermal conductivity of the base fluid is highly conditioned by the decreasing VT^{-2} scaling factor in Equation (2). By introducing the Au nanoplate we are effectively lengthening the mean free-path of thermal vibrations in the system, so that it takes longer for HFAC functions to decay to zero. The integrals from the nanofluid model are notably different, as they peak before meeting a plateau. This proves that a more efficient heat conduction is achieved in presence of the Au nanoplate before it dissipates. The increasing thermal conductivity of the nanofluid with temperature is associated to the sensitivity to temperature of the heat transfer process in solid–liquid interfaces (compared to the base fluid bulk region), as proven by Petravic and Harrowell [72]. As it was

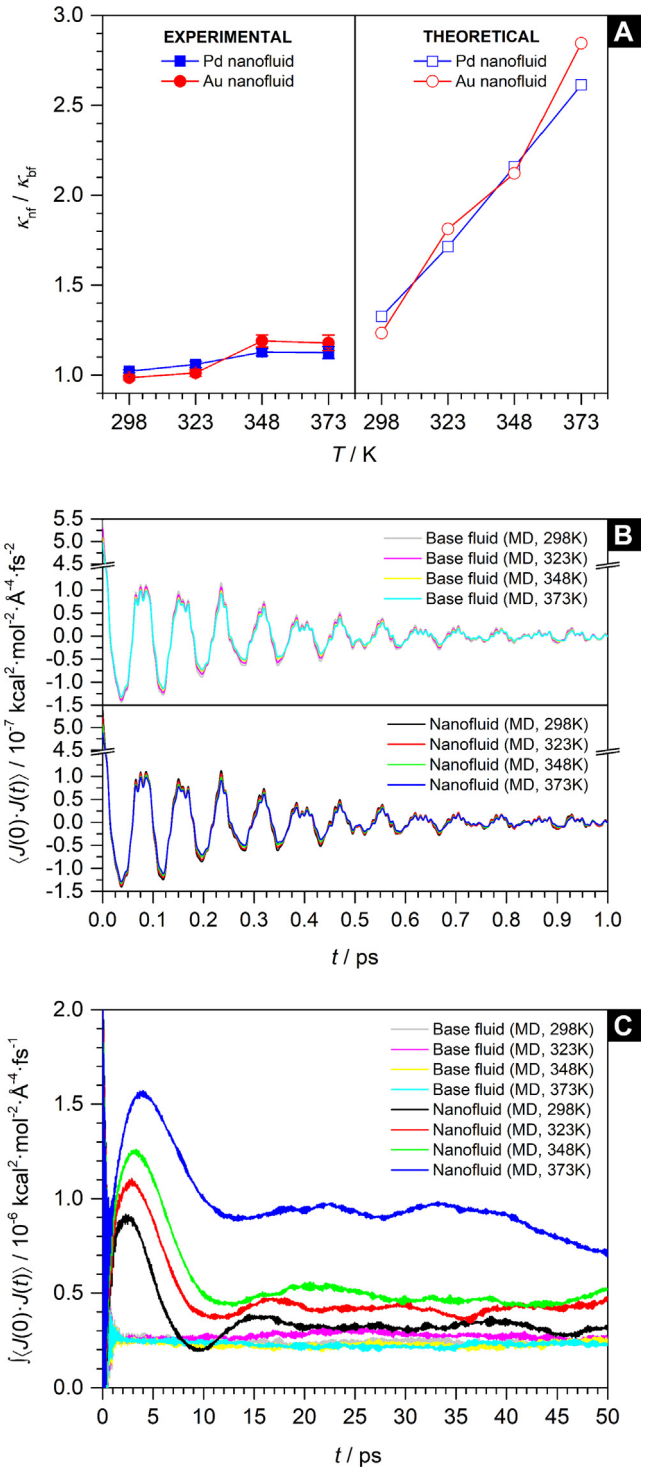

Fig. 7. Experimental and theoretical thermal conductivity enhancements of Pd and Au nanofluids, with respect to the base fluid, as a function of temperature [A], and the HFAC functions [B] and their integrals [C] for the base fluid and the Au nanofluid models at different temperatures (presented in LAMMPS *real* units). Experimental values in [A] are referred to nanofluids with mass fractions of $1.2{\cdot}10^{-2}$ wt% in Pd nanoplates and $1.0{\cdot}10^{-2}$ wt% in Au nanoplates. Solid lines do not represent actual data but are included as guide to the eye.

previously indicated, according to both our experimental and theoretical results, the Au nanoplate-containing nanofluid model is particularly more sensitive to temperature than the Pd nanoplate-containing nanofluid model we studied in a previous work [26]. The presence of chemisorbed species in the case of Pd was proven to distort the nanoplate surface and to act as a high thermal resistance shelter that hinders heat conduction. We suggest that the different nature of the metal and of the atomic interactions at its solid–liquid interface, particularly the absence of chemical bonding at Au surfaces, is responsible of this behaviour with temperature, but further investigation is required.

4. Conclusions

We have presented a comprehensive study of oil-based nanofluids with metal nanoplates and have demonstrated how the chemistry of interfaces defines the thermal properties of these colloids and, consequently, their applicability. The study is purposedly focused on nanofluids prepared using the eutectic and azeotropic mixture of DPO and BP as base fluid. This is the typical HTF in CSP plants, a renewable technology that can benefit from nanofluids to improve the performance of solar-to-thermal-to-electric energy conversion. Understanding how nanomaterials can extraordinarily enhance the thermal properties of the fluid can improve, certainly, its deployment in our energy market.

It has been experimentally proven that the addition of minute mass fraction of Au nanoplates to this base fluid, in the order of 10^{-2} wt%, is sufficient to induce a quantitatively significant change in its thermophysical properties. For instance, with a $4.8{\cdot}10^{-2}$ wt% of Au nanoplates, specific heat and thermal conductivity increase by 6.1 ± 1.4% and 24.9 ± 6.1%, respectively, at 373 K. Our results indicate that the magnitude of the change in these properties is certainly dependent on the surface chemistry of the nanomaterial. DFT simulations reveal that a thermodynamically favoured, kinetically unhindered layer of physisorbed DPO and BP molecules is formed on Au surfaces. The dissimilarities with respect to Pd surfaces are clear, for which DFT simulations predict the formation of a thermodynamically favoured, kinetically restricted layer of chemisorbed biphenyl molecules only. MD simulations in this and previous work has allowed us to propose a relation between the nature of the interactions at the interface and the observed properties of nanofluids: the stronger the interactions between species at solid–liquid interfaces, the higher the specific heat enhancements and the lower the thermal conductivity enhancements at high temperature. More research on additional systems is required to test these propositions, but the evidence provided so far opens new possibilities for research on nanofluids, by providing tentative design principles to tune the physical properties of the nanofluids by choosing solid–liquid pairs with different chemical interactions.

CRediT authorship contribution statement

Iván Carrillo-Berdugo: Conceptualization, Methodology, Investigation, Writing – original draft. **Javier Sampalo-Guzmán:** Investigation. **Ricardo Grau-Crespo:** Conceptualization, Funding acquisition, Writing – review & editing, Supervision. **David Zorrilla:** Formal analysis. **Javier Navas:** Writing – review & editing, Supervision, Project administration, Funding acquisition.

Declaration of Competing Interest

The authors declare that they have no known competing financial interests or personal relationships that could have appeared to influence the work reported in this paper.

Acknowledgements

I.C.-B. thanks *Ministerio de Universidades del Gobierno de España* for endorsing his postdoctoral position at the University of Cadiz with a *Margarita Salas* fellowship, granted within the call for *Recualificación del Sistema Universitario Español para 2021-2023*, funded by the NextGeneration EU programme of the European Union. The group acknowledges Ministerio de Ciencia e Innovación del Gobierno de España for funding under grant RTI2018-096393-B-I00 and for financial support related to the measurement of thermal properties with devices acquired under grant UNCA15-CE-2945. This research was also funded by the Andalucía ERDF Operational Programme 2014-2020, managed by Consejería de Transformación Económica, Industria, Conocimiento y Universidades de la Junta de Andalucía, under grant FEDER-UCA18-107510. This work made use of ARCHER, the UK'S national high-performance computing service, via R.G.-C.'s membership in the HPC Materials Chemistry Consortium, which is funded by EPSRC (EP/R029431), and also of CAI3, the high-performance computing service at *Universidad de Cádiz*.

Appendix A. Supplementary material

Supplementary data to this article can be found online at https://doi.org/10.1016/j.molliq.2022.119762.

References

[1] S.U.S. Choi, J.A. Eastman, Enhancing thermal conductivity of fluids with nanoparticles, in ASME 1995 international mechanical engineering congress & exposition, California, USA, 1995, pp. 99–106.
[2] L. Bo, X. Zhang, Z. Luo, T. Saboori, M. Dehghan, M. Ghasemizadeh, H. Karimi-Maleh, A. Alagumalai, O. Mahian, An overview of the applications of ionic fluids and deep eutectic solvents enhanced by nanoparticles, J. Therm. Anal. Calorim. 147 (14) (2022) 7589–7601.
[3] H. Tyagi, P. Phelan, R. Prasher, Predicted Efficiency of a Nanofluid-Based Direct Absorption Solar Receiver, in ASME 2007 Energy Sustainability Conference (California, USA, 2007), 729-736. 10.1115/ES2007-36139.
[4] R.A. Taylor, P.E. Phelan, T. Otanicar, R.J. Adrian, R.S. Prasher, Vapor generation in a nanoparticle liquid suspension using a focused, continuous laser, Appl. Phys. Lett. 95, 161907 (2009) 1, https://doi.org/10.1063/1.3250174.
[5] T.P. Otanicar, P.E. Phelan, R.S. Prasher, G. Rosengarten, R.A. Taylor, Nanofluid-based direct absorption solar collector, J. Renew. Sustainable Energy 2 033102 (2010) 1, https://doi.org/10.1063/1.3429737.
[6] E. Sani, S. Barison, C. Pagura, L. Mercatelli, P. Sansoni, F. Fontani, D. Jafrancesco, F. Francini, Carbon nanohorns-based nanofluids as direct sunlight absorbers, Opt. Express 18 (2010) 5179, https://doi.org/10.1364/OE.18.005179.
[7] A. Lenert, E.N. Wang, Optimization of nanofluid volumetric receivers for solar thermal energy conversion, Sol. Energy 86 (1) (2012) 253–265.
[8] R. Gómez-Villarejo, E.I. Martín, J. Navas, A. Sánchez-Coronilla, T. Aguilar, J.J. Gallardo, R. Alcántara, D. De los Santos, I. Carrillo-Berdugo, C. Fernández-Lorenzo, Ag-based nanofluidic system to enhance heat transfer fluids for concentrating solar power: nano-level insights, Appl. Energy 194 (2017) 19–29.
[9] J. Navas, P. Martínez-Merino, A. Sánchez-Coronilla, J.J. Gallardo, R. Alcántara, E. I. Martín, J.C. Piñero, J.R. León, T. Aguilar, J.H. Toledo, C. Fernández-Lorenzo, MoS2 nanosheets vs. nanowires: preparation and a theoretical study of highly stable and efficient nanofluids for concentrating solar power, J. Mater. Chem. A 6 (30) (2018) 14919–14929.
[10] T. Aguilar, I. Carrillo-Berdugo, R. Gómez-Villarejo, J.J. Gallardo, P. Martínez-Merino, J.C. Piñero, R. Alcántara, C. Fernández-Lorenzo, J. Navas, A solvothermal synthesis of TiO2 nanoparticles in a non-polar medium to prepare highly stable nanofluids with improved thermal properties, Nanomaterials 8 (1) (2020) 816, https://doi.org/10.3390/nano8100816.
[11] T. Aguilar, E. Sani, L. Mercatelli, I. Carrillo-Berdugo, E. Torres, J. Navas, Exfoliated graphene oxide-based nanofluids with enhanced thermal and optical properties for solar collectors in concentrating solar power, J. Mol. Liq. 306 (1) (2020) 112862, https://doi.org/10.1016/j.molliq.2020.112862.
[12] P. Martínez-Merino, S.D. Midgley, E.I. Martín, P. Estellé, R. Alcántara, A. Sánchez-Coronilla, R. Grau-Crespo, J. Navas, Novel WS2-based nanofluids for concentrating solar power: performance characterization and molecular-level insights, ACS Appl. Mater. Interfaces 12 (5) (2020) 5793–5804.
[13] P. Martínez-Merino, E. Sani, L. Mercatelli, R. Alcántara, J. Navas, WSe2 nanosheets synthesized by a solvothermal process as advanced nanofluids for thermal solar energy, ACS Sustainable Chem. Eng. 8 (3) (2020) 1627–1636.

[14] Concentrating Solar Power Projects, National Renewable Energy Laboratory, U. S. Department of Energy, Office of Energy Efficiency and Renewable Energy (United States of America) (2022), https://solarpaces.nrel.gov.
[15] J. Granatier, P. Lazar, M. Otyepka, P. Hobza, The nature of the binding of Au, Ag, and Pd to benzene, coronene, and graphene: from benchmark CCSD(T) calculations to plane-wave DFT calculations, J. Chem. Theory Comput. 7 (11) (2011) 3743–3755.
[16] P. Keblinski, S.R. Phillpot, S.U.S. Choi, J.A. Eastman, Mechanisms of heat flow in suspension of nano-sized particles (nanofluids), Int. J. Heat Mass Transfer 45 (2002) 855, https://doi.org/10.1016/S0017-9310(01)00175-2.
[17] W. Yu, S.U.S. Choi, An effective thermal conductivity model of nanofluids with a cubical arrangement of spherical particles, J. Nanosci. Nanotechnol. 5 (4) (2005) 580–586.
[18] D. Shin, D. Banerjee, Enhancement of specific heat capacity of high-temperature silica-nanofluids synthesized in alkali chloride salt eutectics for solar thermal-energy storage applications, Int. J. Heat Mass Transfer 54 (5-6) (2011) 1064–1070.
[19] R. Hentschke, On the specific heat capacity enhancement in nanofluids, Nanoscale Res. Lett. 11 (88) (2016) 1, https://doi.org/10.1186/s11671-015-1188-5.
[20] I. Mugica, S. Poncet, A critical review of the most popular mathematical models for nanofluid thermal conductivity, J. Nanopart. Res. 22 (113) (2020) 1, https://doi.org/10.1007/s11051-020-4776-y.
[21] Z. Li, L. Cui, B. Li, X. Du, Mechanism exploration of the enhancement of thermal energy storage in molten salt nanofluid, Phys. Chem. Chem. Phys. 23 (23) (2021) 13181–13189.
[22] E. Leonardi, A. Floris, S. Bose, B. D'Aguanno, Unified description of the specific heat of ionic bulk materials containing nanoparticles, ACS Nano 15 (1) (2021) 563–574.
[23] A. Alagumalai, C. Qin, K.E.K. Vimal, E. Solomin, L. Yang, P. Zhang, T. Otanicar, A. Kaseian, A.J. Chamkha, M.M. Rashidi, S. Wongwises, H.S. Ahn, Z. Lei, T. Saboori, O. Mahian, Conceptual analysis framework development to understand barriers of nanofluid commercialization, Nano Energy 92 (1) (2022) 106736, https://doi.org/10.1016/j.nanoen.2021.106736.
[24] I. Carrillo-Berdugo, S.D. Midgley, R. Grau-Crespo, D. Zorrilla, J. Navas, Understanding the specific heat enhancement in metal-containing nanofluids for thermal energy storage: experimental and ab-initio evidence for a strong interfacial layering effect, ACS Appl. Energy Mater. 3 (9) (2020) 9246–9256.
[25] I. Carrillo-Berdugo, R. Grau-Crespo, D. Zorrilla, J. Navas, Interfacial molecular layering enhances specific heat of nanofluids: evidence from molecular dynamics, J. Mol. Liq. 325 (1) (2020) 115217, https://doi.org/10.1016/j.molliq.2020.115217.
[26] I. Carrillo-Berdugo, P. Estellé, E. Sani, L. Mercatelli, R. Grau-Crespo, D. Zorrilla, J. Navas, Optical and transport properties of metal-oil nanofluids for thermal solar industry: experimental characterization, performance assessment and molecular dynamics insights, ACS Sust. Chem. Eng. 9 (11) (2021) 4194–4205.
[27] Y. Xiong, I. Washio, J. Chen, H. Cai, Z.-Y. Li, Y. Xia, Poly(vinyl pirrolidone): a dual functional reductant and stabilizer of the facile synthesis of noble metal nanoplates in aqueous solutions, Langmuir 22 (2006) 8563, https://doi.org/10.1021/la061323x.
[28] S.S. Shankar, S. Bhargava, M. Sastry, Synthesis of gold nanospheres and nanotriangles by the turkevich approach, J. Nanosci. Nanotechnol. 5 (10) (2005) 1721–1727.
[29] G. Kresse, J. Hafner, Ab initio molecular-dynamics simulation of the liquid-metal-amorphous-semiconductor transition in germanium, Phys. Rev. B 49 (20) (1994) 14251–14269.
[30] G. Kresse, J. Furthmüller, Efficiency of Ab-Initio total energy calculations for metals and semiconductors using a plane-wave basis set, Comput. Mater. Sci. 6 (1) (1996) 15–50.
[31] G. Kresse, J. Furthmüller, Efficient Iterative Schemes for Ab Initio total-energy calculations using a plane-wave basis set, Phys. Rev. B 54 (16) (1996) 11169–11186.
[32] G. Kresse, D. Vogtenhuber, M. Marsman, M. Kaltak, F. Karsai, M. Schlipf. Vienna Ab-initio Simulation Package (VASP), 5.4.4 (2017). https://www.vasp.at.
[33] J.P. Perdew, K. Burke, M. Ernzerhof, Generalized gradient approximation made simple, Phys. Rev. Lett. 77 (18) (1996) 3865–3868.
[34] J.P. Perdew, K. Burke, M. Ernzerhof, Erratum: generalized gradient approximation made simple, Phys. Rev. Lett. 78 (1396) (1997) 1396, https://doi.org/10.1103/PhysRevLett.78.1396.
[35] S. Grimme, J. Antony, S. Ehrlich, H. Krieg, A consistent and accurate Ab initio parametrization of density functional dispersion correction (DFT-D) for the 94 elements H-Pu, J. Chem. Phys. 132 (15) (2010) 154104.
[36] J.A. Garrido Torres, B. Ramberger, H.A. Früchtl, R. Schaub, G. Kresse, Adsorption energies of benzene on close packed transition metal surfaces using the random phase approximation, Phys. Rev. Mater. 1 (1) (2017) 060803, https://doi.org/10.1103/PhysRevMaterials.1.060803.
[37] G. Kresse, J. Hafner, Norm-conserving and ultrasoft pseudopotentials for first-row and transition elements, J. Phys.: Condens. Matter 6 (40) (1994) 8245–8257.
[38] G. Kresse, D. Joubert, From ultrasoft pseudopotentials to the projector augmented-wave method, Phys. Rev. B 59 (3) (1999) 1758–1775.
[39] H.J. Monkhorst, J.D. Pack, Special points for brillouin-zone integrations, Phys. Rev. B 13 (12) (1976) 5188–5192.
[40] J.D. Pack, H.J. Monkhorst, "Special points for Brillouin-zone integrations" – a reply, Phys. Rev. B 16 (4) (1977) 1748–1749.
[41] M. Methfessel, A.T. Paxton, High-precision sampling for brillouin-zone integration in metals, Phys. Rev. B 40 (6) (1989) 3616–3621.
[42] G. Mills, H. Jónsson, G.K. Schenter, Reversible work transition state theory: application to dissociative adsorption of hydrogen, Surf. Sci. 324 (2-3) (1995) 305–337.
[43] H. Jónsson, G. Mills, K.W. Jacobsen. Nudged Elastic Band Method for Finding Minimum Energy Paths of Transitions, in Classical and Quantum Dynamics in Condensed Phase Simulations, 385-404, (1998). 10.1142/3816.
[44] W.L. Jorgensen, J. Tirado-Rives, Potential energy functions for atomic-level simulations of water and organic and biomolecular systems, Proc. Natl. Acad. Sci. U.S.A. 102 (19) (2005) 6665–6670.
[45] L.S. Dodda, J.Z. Vilseck, J. Tirado-Rives, W.L. Jorgensen, 1.14*CM1A-LBCC: localized bond-charge corrected CM1A charges for condensed-phase simulations, J. Phys. Chem. B 121 (15) (2017) 3864–3870.
[46] L.S. Dodda, I. Cabeza de Vaca, J. Tirado-Rives, W.L. Jorgensen, LigParGen Web Server: an automatic OPLS-AA parameter generator for organic ligands, Nucleic Acids Res. 45 (2017) 331, https://doi.org/10.1093/nar/gkx312.
[47] H. Heinz, R.A. Vaia, B.L. Farmer, R.R. Naik, Accurate simulation of surfaces and interfaces of face-centered cubic metals using 12–6 and 9–6 lennard-jones potentials, J. Phys. Chem. C 112 (44) (2008) 17281–17290.
[48] R.C. Lincoln, K.M. Koliwad, P.B. Ghate, Morse-potential evaluation of second- and third-order elastic constants of some cubic metals, Phys. Rev. B 157 (3) (1967) 463–466.
[49] R.C. Lincoln, K.M. Koliwad, P.B. Ghate, Erratum to "morse-potential evaluation of second- and third-order elastic constants of some cubic metals", Phys. Rev. B 162 (3) (1967) 854.
[50] S. Plimpton, Fast Parallel Algorithms for Short-Range Molecular Dynamics, J. Comput. Phys. 117 (1) (1995) 1–19.
[51] S. Plimpton, A. Thompson, S. Moore, A. Kohlmeyer, R. Berger. Large Atomic/Molecular Massively Parallel Simulator (LAMMPS), 17Nov2016 (2016). http://lammps.sandia.gov.
[52] A.I. Jewett, Z. Zhuang, J.-E. Shea, Moltemplate a coarse-grained model assembly tool, Biophys. J. 104 (2013) 169a, https://doi.org/10.1016/j.bpj.2012.11.953.
[53] A. Jewett, Moltemplate 1 (2015) 34.
[54] R.W. Hockney, J.W. Eastwood. Computer Simulation Using Particles. Taylor & Francis Group, 1st ed. (1988).
[55] L. Verlet, Computer "experiments" on classical fluids. I. thermodynamical properties of lennard-jones molecules, Phys. Rev. A 159 (1) (1967) 98–103.
[56] S. Nosé, A molecular dynamics method for simulations in the canonical ensemble, Mol. Phys. 52 (2) (1984) 255–268.
[57] S. Nosé, A unified formulation of the constant temperature molecular dynamics methods, J. Chem. Phys. 81 (1) (1984) 511–519.
[58] W.G. Hoover, Canonical dynamics: equilibrium phase-space distributions, Phys. Rev. A 31 (3) (1985) 1695–1697.
[59] W.G. Hoover, Constant-pressure equations of motion, Phys. Rev. A 34 (3) (1986) 2499–2500.
[60] M.P. Allen, D.J. Tildesley. Computer Simulation of Liquids. Oxford University Press, 2nd ed. (2017).
[61] M.S. Green, Markoff random processes and the statistical mechanics of time-dependent phenomena. II. irreversible processes in fluids, J. Chem. Phys. 22 (3) (1954) 398–413.
[62] R. Kubo, Statistical-mechanical theory of irreversible processes. I. general theory and simple applications to magnetic and conduction problems, J. Phys. Soc. Jpn. 12 (6) (1957) 570–586.
[63] A.R. Tao, S. Habas, P. Yang, Shape control of colloidal metal nanocrystals, Small 4 (3) (2008) 310–325.
[64] Y. Ni, C. Kan, J. Xu, Y. Liu, The synthesis of high yield au nanoplate and optimized optical properties, Superlattices Microstruct. 114 (2018) 124, https://doi.org/10.1016/j.spmi.2017.12.021.
[65] J. Xia, Z. Dong, Y. Cai, G. Guan, S. Zhang, A. Kovács, C. Boothroyd, I.Y. Phang, S. Liu, M. Wu, Y.W. Zhang, X. Hu, M.-Y. Han, Morphological growth and theoretical understanding of gold and other noble metal nanoplates, Chem. - Eur. J. 24 (58) (2018) 15589–15595.
[66] A.V. Naumkin, A. Kraut-Vass, S.W. Gaarenstroom, C.J. Powell. NIST X-ray Photoelectron Spectroscopy Database, in NIST Standard Reference Database 20, Version 4.1, (2012). 10.18434/T4T88K.
[67] J.C. Maxwell. A Treatise on Electricity and Magnetism, Vol. I. Clarendon Press, 1st ed. (1873).
[68] H.G. Raubenheimer, H. Schmidbaur, The late start and amazing upswing in gold chemistry, J. Chem. Educ. 91 (12) (2014) 2024–2036.
[69] J. Jia, H.-S. Wu, Z. Chen, Y. Mo, Elucidation of the forces governing the stereochemistry of biphenyl, Eur. J. Org. Chem. 2013 (3) (2013) 611–616.
[70] A.J.H. McGaughey, M. Kaviany, Thermal conductivity decomposition and analysis using molecular dynamics simulations. part I. lennard-jones argon, Int. J. Heat Mass Transfer 47 (8-9) (2004) 1783–1798.
[71] A.J.H. McGaughey, M. Kaviany, Thermal conductivity decomposition and analysis using molecular dynamics simulations: part II. complex silica structures, Int. J. Heat Mass Transfer 47 (8-9) (2004) 1799–1816.
[72] J. Petravic, P. Harrowell, Equilibrium calculations of viscosity and thermal conductivity across a solid-liquid interface using boundary fluctuations, J. Chem. Phys. 128 (1) (2008) 194710, https://doi.org/10.1063/1.2911924.